Solid State Communications 181 (2014) 9–14

Contents lists available at ScienceDirect

Solid State Communications

journal homepage: www.elsevier.com/locate/ssc

Impurity and morphological dependence on photoluminescence and enhanced impurity-induced two-photon absorption in ZnO

Daniel J. Clark [a], Lu Yuan [b], Calford O. Otieno [a], Guangwen Zhou [b], Joon I. Jang [a,*]

[a] Department of Physics, Applied Physics and Astronomy, Binghamton University P.O. Box 6000, Binghamton, NY 13902 USA
[b] Department of Mechanical Engineering, Binghamton University P.O. Box 6000, Binghamton, NY 13902 USA

ARTICLE INFO

Article history:
Received 11 October 2013
Received in revised form
5 November 2013
Accepted 15 November 2013
by M. Grynberg
Available online 22 November 2013

Keywords:
A. ZnO
D. Exciton
E. Photoluminescence
E. Nonlinear optics

ABSTRACT

In this study, we characterize the relative crystal quality of zinc oxide (ZnO) synthesized at various temperatures via photoluminescence (PL) measurements. By varying the oxidation temperature during the growth process, different sample morphologies arise. These structural differences cause changes in the PL spectra which allow us to gain insight into the crystal purity. We employ three independent spectroscopic methods to examine ZnO prepared with various morphologies; time-integrated PL, random lasing, and time-resolved PL. As a result of the impurity band being resonant with the two-photon absorption (2PA) range, multifold enhanced 2PA is observed and the 2PA coefficient is measured to be 2500 cm/GW for tetrapod ZnO at 613 nm.

1. Introduction

Zinc oxide (ZnO) is a wide-bandgap type II–VI semiconductor with a hexagonal wurtzite structure with no inversion symmetry [1]. It has a direct bandgap of $E_g = 3.37$ eV at 300 K [2]. ZnO is a versatile material with a myriad applications including solar cells, varistors, spintronic devices, photodetectors, light emitting diodes, and thin film gas sensors [1,3–5]. ZnO has also been used as an active layer in various heterogeneous quantum well nanostructures [6]. In order to improve its beneficial properties, numerous attempts have been made to develop various ZnO structures that include thin films, nanorods, and nanowires [7,8]. The design process, however, typically introduces imperfections (structural or stoichiometric) in ZnO. Since the efficiencies of ZnO-based devices critically depend on the quality of the host material, it is important to control and/or find an optimal growth condition for high-quality ZnO crystals.

Various morphologies of ZnO can be fabricated depending on the oxidation temperature and growth process [7,9]. One particular morphology of interest is the ZnO tetrapod. It has applications ranging from optical to antibacterial [10] and exhibits extended exciton lifetimes [11,12]. Its electromagnetic properties make it an ideal candidate for use as a radar absorbing material [13]. The non-destructive technique of photoluminescence (PL) can investigate the effects arising from morphological changes in ZnO, which includes changes in crystallinity. Optical excitation of this semiconductor across the bandgap leads to the formation of tightly-bound excitons at room temperature with a large exciton binding energy of ~60 meV [14]. This often yields room-temperature stimulated emission as well as lasing under a moderate excitation level [15,16]. The mechanism for PL emission varies but can be excitonic, impurity-induced, or structural. This study investigates PL from nanostructured and tetrapod ZnO. We characterize sample purity across different oxidation temperatures in the fabrication process by comparing band-to-band emission intensity to that of impurity-induced emission, by estimating the random lasing cavity distance, [17,18] and by measuring the exciton recombination lifetime via time-resolved photoluminescence (TRPL).

We also determine the two-photon absorption (2PA) coefficient in tetrapod ZnO based on PL techniques. Although high impurity concentration in a condensed matter system is generally considered as a drawback, we show that a broad impurity band in ZnO tetrapod, which is resonant with the 2PA band, immensely increases the 2PA efficiency. This implies that tetrapod ZnO powder in a suspension form has a potential for optical limiting applications [19,20] together with additional merits in optical transparency over the visible and IR ranges. We believe that the effect is universal in which an impurity level can play an important role as a "real" intermediate state, which would highly enhance the 2PA cross-section.

2. Sample preparation and characterizations

High-purity Zn foils (99.99%) with a thickness of 0.25 mm obtained from Sigma-Aldrich are used in this experiment.

* Corresponding author. Tel.: +1 607 777 4279.
E-mail address: jjoon@binghamton.edu (J.I. Jang).

0038-1098/$ - see front matter © 2013 Elsevier Ltd. All rights reserved.
http://dx.doi.org/10.1016/j.ssc.2013.11.020

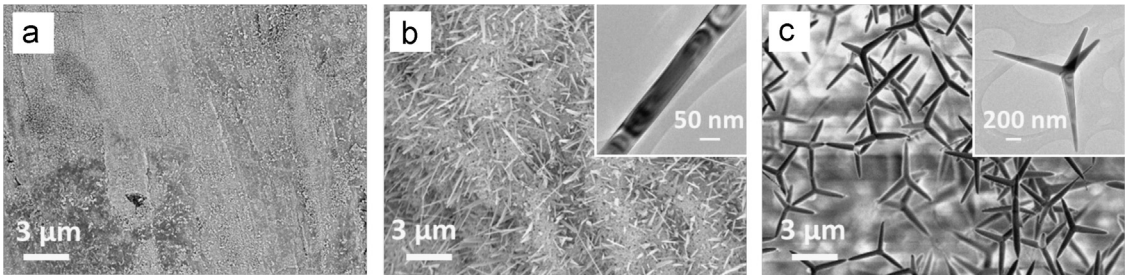

Fig. 1. SEM images of the oxidized Zn surface at different temperatures: (a) 300 °C, (b) 500 °C, and (c) 1000 °C. The insets show the TEM images of a typical ZnO nanowire and tetrapod, respectively.

Gold-coated (~10 nm) Si wafers with (111) orientation serve as the deposition substrate. A chromium primer layer (~2 nm) is coated before gold coating to improve adhesion between the gold layer and the Si substrate. ZnO nanostructures are grown in a horizontal furnace with pure oxygen (99.999%) as a reaction gas. The Zn samples are first thoroughly rinsed with deionized water and then ultrasonicated in acetone for 5 min. The cleaned Zn substrates are dried in an N_2 environment and then placed in a ceramic boat while the Si substrates are placed in another ceramic boat. Both ceramic boats are placed into the horizontal furnace with Si substrates upstream along the gas flow. The furnace is flowed with 100 sccm (standard cubic centimeter per minute) argon gas for 5 min and then rapidly heated from room temperature to the desired temperature (200–1000 °C) in 10 min with argon gas flow. The gas is immediately switched to pure oxygen with a 100 sccm flow rate and maintained for 30 min. The furnace is then naturally cooled to room temperature.

The as-synthesized products are characterized by field-emission scanning electron microscopy (FEG-SEM, FEI Supra 55VP), X-ray diffraction (XRD, PANalytical's X'Pert), and transmission electron microscopy (JEOL 2100F TEM) operated at 200 kV. The PL experiments are conducted on Zn substrates oxidized between 200 °C and 800 °C. The gray powder formed on the Si substrate at 1000 °C is also collected for the PL measurements.

It is evident from SEM observations that there are no ZnO structures formed on the surface at relatively low temperatures (200 °C and 300 °C) [see Fig. 1(a)]. At temperatures between 400 °C and 800 °C the Zn substrates are covered with ZnO nanowires. The length and diameter of the nanowires increase with the oxidation temperature. Fig. 1(b) shows that densely-packed ZnO nanowires are formed on the surface at 500 °C with ~50 nm in width and ~1.5 μm in length. The inset image of Fig. 1 (b) illustrates a bright-field TEM image of a single ZnO nanowire with a very smooth surface. It is however found that the melting of Zn (a melting temperature of ~420 °C) causes the surface of Zn to become rough at 500 °C.

Since the boiling temperature of Zn is 907 °C, the Zn foil totally disappears after oxidation at 1000 °C for 30 min. Meanwhile, the Si substrate is covered by a gray thin layer. The SEM image of the Si substrate in Fig. 1(c) shows highly uniform ZnO tetrapods formed on the surface. Each ZnO tetrapod contains four legs with smooth surfaces and a sharp tip at the end as depicted in the inset of Fig. 1(c).

Fig. 2 shows the representative XRD patterns of Zn oxidized at different temperatures. Pattern (a) is obtained from ZnO powder deposited on the Si substrate at 1000 °C. The diffraction peaks can be ascribed to the hexagonal wurtzite structure of ZnO with no contribution from Zn due to complete evaporation. The peaks in pattern (c) match well with Zn, implying that there are few ZnO species formed at 300 °C. Samples grown at the intermediate temperatures yield dual phases of Zn and ZnO.

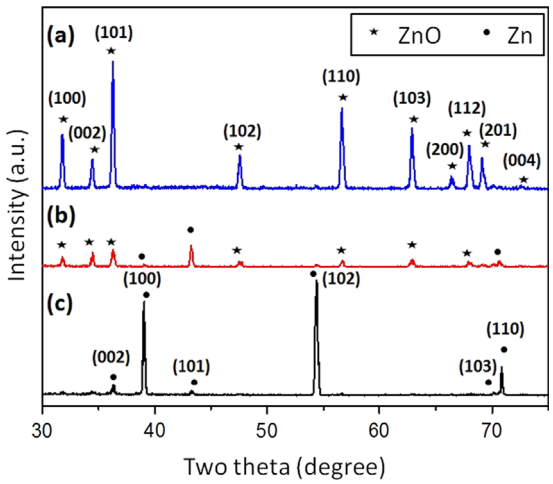

Fig. 2. (Color online) XRD patterns of Zn oxidized at (a) 1000 °C, (b) 500 °C, and (c) 300 °C.

3. Photoluminescence experiments

Our PL experiments are all conducted at room temperature. One-photon-induced PL of the ZnO samples is probed with the frequency-tripled output (355 nm) from an EKSPLA PL-2250 series Nd:YAG laser with a repetition rate of 50 Hz and a 30 ps pulse width. This laser also synchronously pumps an EKSPLA PG 403 optical parametric oscillator (OPO) to generate continuously tunable coherent radiation from 210 nm to 2300 nm. Two-photon-induced PL is measured with either the frequency-doubled output (532 nm) of the YAG laser or the OPO tuned to $\lambda = 613$ nm.

The excitation beam is focused onto the sample using a positive lens ($f = 7.5$ cm) and the corresponding spot size is directly measured to estimate the input fluence if required. The PL signal is collected onto a fiber-optic bundle in a reflection geometry with a combination of collection lenses. Time-integrated PL signals of the ZnO samples are spectrally resolved through the use of a fiber-optic cable coupled to a selective-grating Horiba iHR320 spectrometer equipped with a charge-coupled device (CCD) camera.

Exciton lifetimes are measured via TRPL using the same frequency-tripled output of the Nd:YAG laser as an excitation source. The PL emission is collected in a reflection geometry and focused into another Horiba iHR320 spectrometer. Fiber-optic cables are not employed as they can cause artifacts resulting from fiber modal dispersion. The spectrally-resolved PL is then time-resolved with a C10627 Hamamatsu Streak Scope with a 5 ps resolution coupled to a C9300 Hamamatsu Digital CCD Camera.

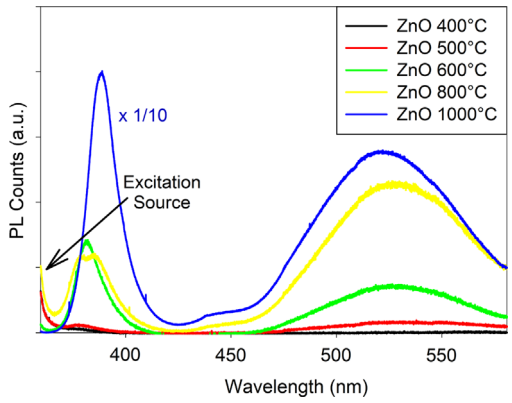

Fig. 3. (Color online) PL spectra of ZnO oxidized at various oxidation temperatures. The PL counts of 390 nm emission and impurity-induced emission (520 nm) increase for higher oxidation temperatures.

4. Spectral features of ZnO under one-photon excitation

The time-integrated PL spectra from the ZnO samples under one-photon excitation with a constant input power of 0.3 MW are shown in Fig. 3. Samples oxidized below 400 °C exhibit no measureable PL, which is consistent with Section 2. In general, the measured PL counts increase with oxidation temperature. The higher-energy tail is remnant from the excitation source (355 nm). Peaks near 390 nm, corresponding to near-band-edge (NBE) emission, are seen to increase in intensity with higher oxidation temperatures. A slight disparity in the spectral positions of NBE emission most likely arises due to varying degrees of built-in stress and sample morphologies in each sample. This can also cause splitting of the PL peak (see for example the yellow trace) [6,21]. The energy splitting in the NBE peak is about 53.6 meV which is due to a local stress estimated to be 1.8 GPa [22]. However, noticeably increased and redshifted PL from ZnO tetrapods (blue trace) arises from high-density excitons with a longer exciton lifetime as discussed in Section 5.

The origin of the broader PL peak below NBE emission arises from radiative recombination of photo-generated holes with the singly ionized charge state of an oxygen vacancy [23]. This impurity peak is also seen to increase in intensity with higher oxidation temperatures. The observed trend indicates that the overall PL efficiency increases with higher oxidation temperatures. This is indeed consistent with Section 2, since higher oxidation temperatures yield more compact ZnO structures that in turn increase the effective excitation area (more ZnO is illuminated). Therefore, we should not determine the sample quality simply based on the PL counts but the *ratio* of NBE to impurity-induced emission.

For the samples with oxidation temperatures of 600 °C and above, the strong NBE emission peak in Fig. 3 is caused by inelastic scattering of two thermal excitons. One exciton rapidly recombines near the polariton bottleneck, leaving the other in a higher energy state by conserving both energy and momentum, known as the P-band [24]. For samples with lower oxidation temperatures, the less intense and broader peak observed is due to radiative recombination of excitons (X-band). Since these samples contain relatively sparse ZnO nanostructures, lower oxidation temperatures inhibit the occupation of a large exciton density, thus suppressing exciton–exciton scattering. P-band emission is observed more readily for higher oxidation temperatures within a lower input energy range (see Fig. 5).

Power dependences are carried out for the NBE emission peak for each sample whereby the PL counts are recorded as a function of input energy; here the corresponding fluence or intensity is not estimated for scattered ZnO nanostructures spread over the substrates since the effective illumination area of the samples is not known precisely. Under low-energy one-photon excitation, all samples exhibit a linear power dependence (X-band). Stimulated P-band emission is also observed as we increase the pulse energy, and the corresponding power dependence becomes superlinear.

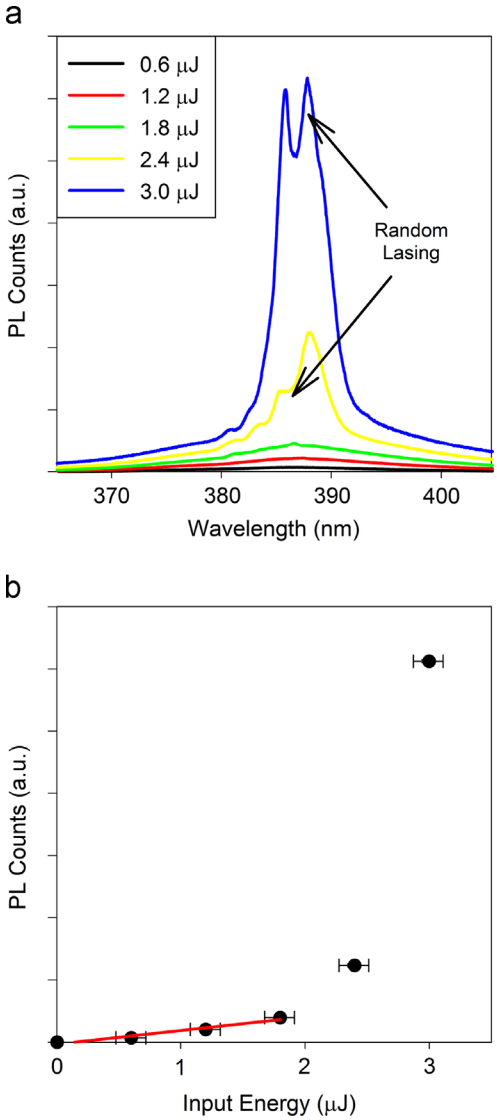

Fig. 4. (Color online) (a) NBE emission spectra from ZnO oxidized at 800 °C under several excitation levels. (b) Spectrally-integrated PL counts vs. input energy (dots). Stimulated emission occurs near 2 μJ pulses. The solid red line indicates the range for X-band emission.

For example, Fig. 4(a) plots several time-integrated NBE emission spectra from ZnO grown at 800 °C, when the pulse energy is varied in the range of 0.6–3.0 μJ. Sharp peaks on top of the PL spectra are attributed to random lasing. This quantum mechanical phenomenon is an indication of sample quality as impurities can act as scattering sites in which they form random cavities for specific wavelengths of PL emission to lase [17,18]. This allows us to determine the sample quality as detailed in Section 5. The dots in Fig. 4(b) are the spectrally-integrated PL counts from part (a) plotted as a function of pulse energy. The onset of stimulated emission is evident as indicated by a significant deviation from a linear fit (red line).

Fig. 5 is a plot of the highest input energy where linear power dependence is observed (i.e. just below the onset of P-band) as a function of oxidation temperature. It is clear that bigger ZnO

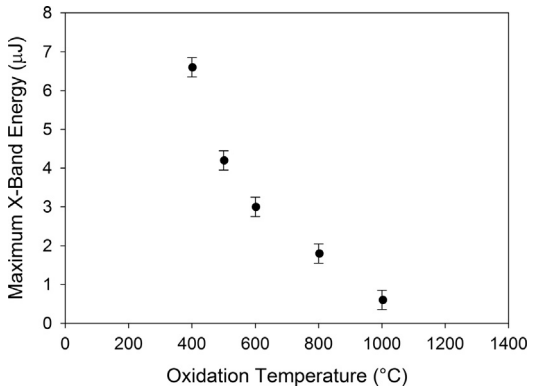

Fig. 5. Pulse energy just below the P-band onset vs. oxidation temperature. This directly reveals the size effects that tend to suppress P-band emission in smaller nanostructured ZnO.

structures grown at higher oxidation temperatures yield more efficient scattering of excitons leading to P-band emission. In other words, higher onset energies are required for P-band emission in ZnO grown at lower temperatures. Our observation is consistent with the previous study that reports on suppression of P-band emission in smaller ZnO nanostructures due to a more reduced density of states near the bottleneck [25].

5. Characterization of ZnO quality via spectroscopic techniques

In order to further characterize the crystal quality, we examine random lasing in our samples. All ZnO samples display random lasing in their one-photon-induced PL spectra [see for example Fig. 4(a) and Fig. S1(a) in Suppl.]. The spectral distance between successive random lasing peaks overlaid on the exciton emission peak is used to determine sample quality with respect to the other samples. By taking a Fourier transform (FT) of the wavenumber spectrum, random lasing cavity length can be determined by the harmonic separation in the FT spectrum, $n_0 L/\pi$, where $n_0 = 2.1$ is the linear refractive index of ZnO and L is the cavity length [18]. This length can then be used to determine impurity density since longer cavity lengths imply larger spacing between impurity sites or less total number of impurities.

Fig. S1 shows (a) the PL spectrum plotted in wavenumber along with (b) its FT spectrum measured from ZnO oxidized at 400 °C. The corresponding cavity length is $L = 23 \pm 2$ μm. The experimental L values of our samples are shown in Table 1, indicating that oxidation at 600 °C is an optimal condition for high-quality ZnO.

This random-lasing method is confirmed by another independent method. Also in Table 1, we present the ratio of NBE emission to impurity-induced emission obtained from Fig. 3. Note that both methods yield similar trends and ZnO (600 °C) shows the highest NBE/impurity emission ratio, again indicating high-quality ZnO.

Finally, exciton lifetimes are measured via TRPL to determine crystal quality. In general, longer lifetimes imply better crystal quality since fewer impurities are present to act as additional recombination sites. For example, Fig. S2(a) in Suppl. exhibits the TRPL spectra observed from ZnO (1000 °C). The PL transient $N(t)$ is generated by spectrally integrating the corresponding TRPL spectra and plotted in Fig. S2(b) on a semi-logarithmic (semi-log) scale. Because of different decay times for spectrally overlapping X-band and P-band emission, the observed transient exhibits a bi-exponential decay [12,26].

Table 2 shows p-band lifetime $|\tau_p|$ and x-band lifetime $|\tau_x|$ determined from fits. All samples exhibit similar P-band lifetimes,

Table 1
Two methods of determining crystal quality; random lasing method and time-integrated PL method. Both methods yield similar trends, indicating that ZnO oxidized at 600 °C is of the best crystalline quality.

Oxidation temp. (°C)	L (μm)	Peak ratio
400	23.17 ± 0.02	0.562 ± 0.142
500	24.69 ± 0.95	0.338 ± 0.018
600	54.58 ± 2.80	1.800 ± 0.030
800	22.39 ± 0.78	0.319 ± 0.004
1000	24.17 ± 0.87	0.607 ± 0.007

Table 2
Characteristic exciton lifetimes for P-band and X-band.

Oxidation temp. (°C)	P-band (ps)	X-band (ps)
500	7.64 ± 0.08	75.53 ± 12.29
600	7.89 ± 0.07	73.48 ± 9.27
800	9.08 ± 0.10	83.29 ± 9.65
1000	8.47 ± 0.06	297.10 ± 29.95

however, the tetrapod ZnO shows an extended X-band lifetime compared to the nanostructured ZnO. This longer lifetime in the tetrapods is a result of reduced surface effects caused by the sample morphology. These surface effects play a significant role in assisting the recombination processes. Since the tetrapods have smaller surface to volume ratios, they exhibit extended exciton lifetimes as compared to structurally smaller nanowires formed at lower oxidation temperatures [27]. P-band lifetimes are very short (~8 ps), implying highly efficient coupling of excitons with photons near the bottleneck. The measured P-band lifetimes may in fact be shorter since the experimental τ_p is comparable to the resolution of the streak camera (~5 ps).

The overall decay rate experimentally measured is given by $\Gamma = \Gamma_{radiative} + \Gamma_{impurity}$. From our TRPL measurements we conclude that intrinsic decay rates for P-band and X-band are faster than $\Gamma_{impurity}$ and that $\Gamma_{radiative}$ is the dominating term since there is little fluctuation in P-band lifetimes among all morphologies. Also, a sudden increase in the X-band lifetime is typical of a tetrapod morphology, which cannot be directly related to the level of impurity concentration. Therefore, the method of determining sample purity with TRPL seems not viable in our case. Using TRPL as a method of determining sample purity may only work in a specific regime where $\Gamma_{radiative}$ is comparable to (or slower than) $\Gamma_{impurity}$.

6. Highly-enhanced impurity-induced 2PA

2PA occurs as a consequence of simultaneous absorption of two photons that induces electronic excitation of a semiconductor under the condition $E_g/2 \leq \hbar\omega \leq E_g$. It is a nonlinear optical process that depends quadratically on the input intensity I and parametrized by the 2PA coefficient β. Being a higher-order nonlinear process, 2PA is typically several orders of magnitude weaker than linear absorption. Unlike one-photon excitation, 2PA is a "volume excitation" in which the absorption length is given by $(\beta I)^{-1}$. Therefore, a test sample should have a sufficient dimension especially under picosecond excitation. Only the ZnO sample oxidized at 1000 °C is two-photon active in our experimental condition. As predicted, the experiment confirms that two-photon-induced PL increases with I^2 below the onset of stimulated emission.

Conventionally, a single-beam Z-scan technique [28] has been employed to estimate β of a nonlinear material prepared into film or bulk forms. Since our ZnO tetrapods are powdered, we measure

β by estimating the absolute exciton density near Mott transition [29]. We approximate the absolute value of β at $\lambda=$ 613 nm by comparing the experimental exciton density at Mott transition with the theoretical Mott density n_{Mott}.

The population and relaxation kinetics of X-band and P-band excitons can be modeled by coupled rate equations [30];

$$\frac{dn_x}{dt} = G_2 - \frac{n_x}{\tau_x} - An_x^2, \tag{1}$$

$$\frac{dn_p}{dt} = An_x^2 - \frac{n_p}{\tau_p}, \tag{2}$$

where n_x and n_p are densities of X-band and P-band excitons, and A is an exciton–exciton scattering coefficient associated with P-band emission. Any impurity-induced recombination is neglected as discussed in Section 5. Since the excitation pulse width and the decay time of the P-band excitons (measured by TRPL) are similar, we consider the system to be in quasi-steady state. The steady-state solution to Eqs. (1) and (2) under high excitation levels ($n_x/\tau_x \ll An_x^2$) is given by $n_p = \tau_p G_2 = \tau_p \beta I^2/2\hbar\omega$.

When the inter-particle distance approaches the exciton Bohr radius, Mott transition occurs. At this point, the pairwise correlation in a single exciton is lost and an electron-hole plasma (EHP) emerges. This can be experimentally probed since stimulated emission is strongly suppressed due to the fermionic nature of the EHP. Fig. 6(a) shows a series of time-integrated PL spectra as we increase the pulse energy from 19.5 μJ to 112 μJ. The EHP phase is evident from peak broadening as well as redshift under high excitation levels. We plot the corresponding spectrally-integrated PL counts (dots) as a function of pulse energy in Fig. 6(b) on a semi-log scale. The two lines indicate the observed power dependence for excitonic and EHP emission. The crossover approximately corresponds to the Mott density. Using $n_p = \tau_p G_2 = n_{Mott} \sim a_B^{-3}$, we can calculate β;

$$\beta = \frac{2\hbar\omega}{I^2 \tau_p a_B^3} = 2500 \pm 250 \text{ cm/GW}, \tag{3}$$

where I ($\sim$2 GW/cm^2) is the input intensity at the onset of Mott transition, a_B=2.34 nm is the exciton Bohr radius [31], and ω is the angular frequency of 613 nm photons. Note that this β value is 500 times larger than that in bulk ZnO (5.0 cm/GW at 532 nm [32]) and about three orders of magnitude larger than a theoretical value at 613 nm, predicted by a two-band model [28].

What causes such a strongly enhanced 2PA process? Although optical nonlinearity is known to increase in many semiconducting nanostructures [33,34], any quantum-size effect is unlikely considering the physical dimension of our ZnO tetrapods [see Fig. 1(c)]. Since 2PA always involves intermediate states, the observed enhancement most likely arises due to a resonance effect. In fact, highly efficient 2PA in ZnO was previously reported near excitonic resonance [35]. Since our experimental 2PA wavelength is resonant with the broad impurity band (see Fig. 3), we believe that this band enhances the 2PA coefficient by supplying a "real" intermediate state for this nonlinear process to occur much more effectively.

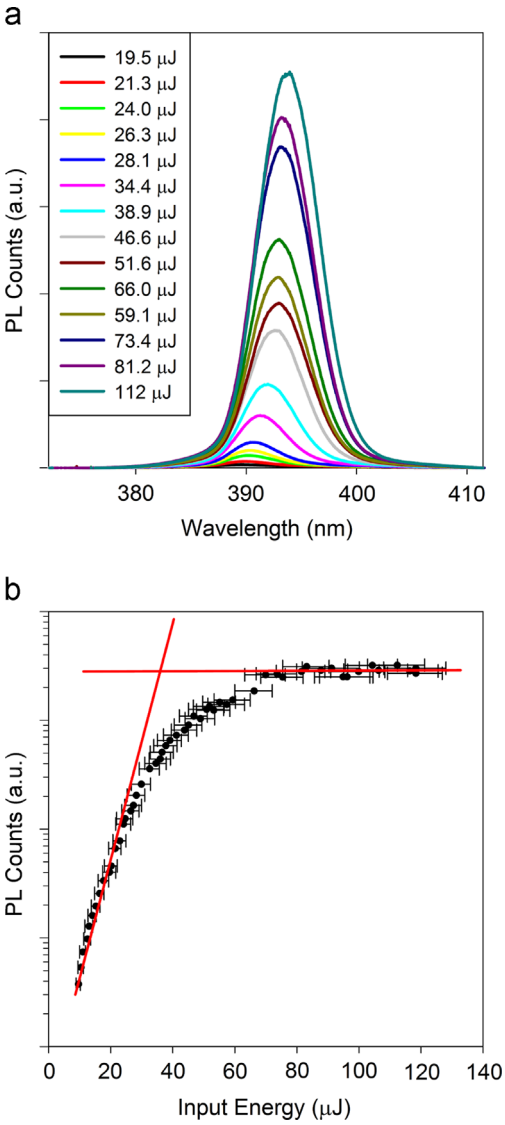

Fig. 6. (Color online) (a) Time-integrated PL spectra vs. pulse energy. (b) Spectrally-integrated PL counts vs. pulse energy. Mott transition occurs at the crossover of the two red lines.

7. Conclusions

We have studied the effect of oxidation temperature on the PL properties of ZnO essentially arising from different sample morphologies. We have determined relative crystal quality via three independent spectroscopic methods. In our case, TRPL is not a suitable technique because of rapid radiative recombination of excitonic matter. We have reached the conclusion that the purest ZnO sample is oxidized at 600 °C. Our spectroscopic techniques can be used for characterizing the quality of materials exhibiting PL responses.

The tetrapod ZnO shows not only the longest X-band exciton lifetime among all the samples, but also significantly enhanced 2PA-induced PL. Due to the high level of impurities in tetrapod ZnO, 2PA is resonantly enhanced in comparison to bulk ZnO having much higher sample quality in general. In order to explain the strongly enhanced TPA coefficient, we will experimentally determine the lifetime broadening (Γ) of the associated impurity level and theoretically calculate the resonance effect in the 2PA matrix elements.

Acknowledgments

GZ would like to acknowledge the supports of NSF Grant nos. CMMI-0825737 and CMMI-1056611. DJC would like to acknowledge the support of the K. Keith Innes Research Grant.

Appendix A. Supplementary material

Supplementary data associated with this article can be found in the online version at http://dx.doi.org/10.1016/j.ssc.2013.11.020.

References

[1] M. Wang, K.E. Lee, S.H. Hahn, E.J. Kim, S. Kim, J.S. Chung, E.W. Shin, C. Park, Mater. Lett. 61 (2007) 1118–1121.
[2] G. Petrov, V. Shcheslavskiy, V. Yakovlev, I. Ozerov, E. Chelnokov, W. Marine, in: Quantum Electronics and Laser Science, QELS Postconference Digest, 2003, p. 2.
[3] T. Söderström, F.-J. Haug, X. Niquille, V. Terrazzoni, C. Ballif, Appl. Phys. Lett. 94 (2009) 063501.
[4] S. Faÿ, U. Kroll, C. Bucher, E. Vallat-Sauvain, A. Shah, Sol. Energy Mater. Sol. Cells 86 (2005) 385–397.
[5] X. Ju, W. Feng, X. Zhang, V. Kittichungchit, T. Hori, H. Moritou, A. Fujii, M. Ozaki, Sol. Energy Mater. Sol. Cells 93 (2009) 1562–1567.
[6] H. Matsui, H. Tabata, New Developments in Photon and Materials Research, Nova Science Publishers, Inc., 2013.
[7] W. Tan, K.A. Razak, K. Ibrahim, Z. Lockman, J. Alloys Compd. 509 (2011) 6806–6811.
[8] S. Anas, R. Mangalaraja, S. Ananthakumar, J. Hazard. Mater. 175 (2010) 889–895.
[9] M. Aida, E. Tomasella, J. Cellier, M. Jacquet, N. Bouhssira, S. Abed, A. Mosbah, Thin Solid Films 515 (2006) 1494–1499.
[10] J. Tawale, K. Dey, R. Pasricha, K. Sood, A. Srivastava, Thin Solid Films 519 (2010) 1244–1247.
[11] Y. Zhong, A.B. Djurisic, Y.F. Hsu, K.S. Wong, G. Brauer, C.C. Ling, W.K. Chan, J. Phys. Chem. C 112 (2008) 16286–16295.
[12] S.-K. Lee, S.L. Chen, D. Hongxing, L. Sun, Z. Chen, W.M. Chen, I.A. Buyanova, Appl. Phys. Lett. 96 (2010) 083104.
[13] B. Caudle, G. Flowers, M. Baginski, S. Wentworth, S. Rao, in: 2013 IEEE International Conference on Microwaves, Communications, Antennas and Electronics Systems (COMCAS), pp. 1–4.
[14] R.C. Rai, M. Guminiak, S. Wilser, B. Cai, M.L. Nakarmi, J. Appl. Phys. 111 (2012) 073511.
[15] A.-S. Gadallah, K. Nomenyo, C. Couteau, D.J. Rogers, G. Lérondel, Appl. Phys. Lett. 102 (2013) 171105.
[16] C.F. Zhang, Z.W. Dong, K.J. Liu, Y.L. Yan, S.X. Qian, H. Deng, Appl. Phys. Lett. 91 (2007) 142109.
[17] J. Fallert, R. Dietz, M. Hauser, F. Stelzl, C. Klingshirn, H. Kalt, J. Lumin. 129 (2009) 1685–1688.
[18] H.-C. Hsu, C.-Y. Wu, W.-F. Hsieh, J. Appl. Phys. 97 (2005) 064315.
[19] M. Sheik-Bahae, E.W. Van Stryland, A.A. Said, D.J. Hagan, M.J. Soileau, Opt. Eng. 30 (1991) 1228–1235.
[20] J. Wang, W.J. Blau, J. Opt. A: Pure Appl. Opt. 11 (2009) 024001.
[21] Q. Yan, P. Rinke, M. Winkelnkemper, A. Qteish, D. Bimberg, M. Scheffler, C.G. Van de Walle, Appl. Phys. Lett. 101 (2012) 152105.
[22] W. Shan, W. Walukiewicz, J.W. Ager, K.M. Yu, Y. Zhang, S.S. Mao, R. Kling, C. Kirchner, A. Waag, Appl. Phys. Lett. 86 (2005) 153117.
[23] K. Vanheusden, W.L. Warren, C.H. Seager, D.R. Tallant, J.A. Voigt, B.E. Gnade, J. Appl. Phys. 79 (1996) 7983–7990.
[24] J. Jang, S. Park, N. Frazer, J. Ketterson, S. Lee, B. Roy, J. Cho, Solid State Commun. 152 (2012) 1241–1243, See also Ref. 29 for an alternative explanation.
[25] R. Hauschild, H. Lange, H. Priller, C. Klingshirn, R. Kling, A. Waag, H.J. Fan, M. Zacharias, H. Kalt, Phys. Status Solidi (b) 243 (2006) 853–857.
[26] W.M. Kwok, A.B. Djurišić, Y.H. Leung, W.K. Chan, D.L. Phillips, Appl. Phys. Lett. 87 (2005) 223111.
[27] J.S. Reparaz, F. Güell, M.R. Wagner, A. Hoffmann, A. Cornet, J.R. Morante, Appl. Phys. Lett. 96 (2010) 053105.
[28] M. Sheik-Bahae, A. Said, T.-H. Wei, D. Hagan, E.W. Van Stryland, IEEE J. Quantum Electron. 26 (1990) 760–769.
[29] C. Klingshirn, R. Hauschild, J. Fallert, H. Kalt, Phys. Rev. B 75 (2007) 115203.
[30] S. Mani, J.I. Jang, J.B. Ketterson, Appl. Phys. Lett. 93 (2008) 041902.
[31] R.T. Senger, K.K. Bajaj, Phys. Rev. B 68 (2003) 045313.
[32] M. Weber, Optical Materials, vol. 7, in: CRC Handbook of Laser Science and Technology, Supplement 2, CRC Press, 1995.
[33] S. Shi, S. Xu, Z.-X. Xu, V. Roy, C.-M. Che, Chem. Phys. Lett. 506 (2011) 226–229.
[34] L. Irimpan, V.P.N. Nampoori, P. Radhakrishnan, B. Krishnan, A. Deepthy, J. Appl. Phys. 103 (2008) 033105.
[35] Y.-P. Chan, J.-H. Lin, C.-C. Hsu, W.-F. Hsieh, Opt. Express 16 (2008) 19900–19908.